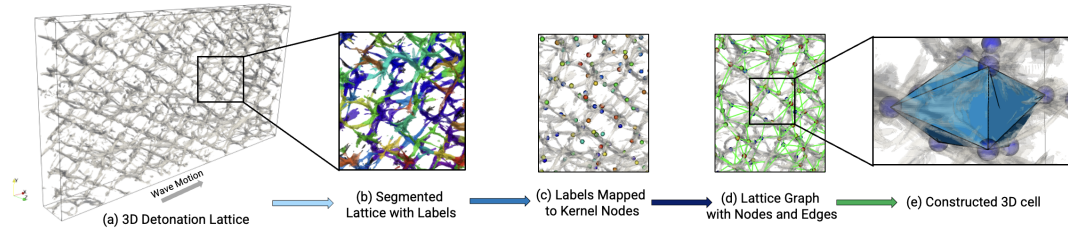


An approximate graph elicits detonation lattice

Vansh Sharma^{a,*} and Venkat Raman^a

^aDepartment of Aerospace Engineering, University of Michigan, Ann Arbor, MI 48109-2102, USA



Abstract

This study presents a novel algorithm based on graph theory for the precise segmentation and measurement of detonation cells from 3D pressure traces, termed detonation lattices, addressing the limitations of manual and primitive 2D edge detection methods prevalent in the field. Using a segmentation model, the proposed training-free algorithm is designed to accurately extract cellular patterns, a longstanding challenge in detonations research. First, the efficacy of segmentation on generated data is shown with a prediction error 2%. Next, 3D simulation data is used to establish performance of the graph-based workflow. The results of statistics and joint probability densities show oblong cells aligned with the wave propagation axis with 17% deviation, whereas larger dispersion in volume reflects cubic amplification of linear variability. Although the framework is robust, it remains challenging to reliably segment and quantify highly complex cellular patterns. However, the graph-based formulation generalizes across diverse cellular geometries, positioning it as a practical tool for detonation analysis and a strong foundation for future extensions in triple-point collision studies.

Keywords: 3D Detonation; Soot Foil; Graph; Cell Classification; Cellular Detonation; Detonation Lattice; SAM Model

Novelty and significance statement

Detonation cells are key features of canonical propagating waves, and are useful for understanding cellular instabilities. Currently, there is very limited work on methods for estimating cell sizes, with manual counting in two-dimensions being the common approach. Existing numerical approaches typically work with 2D data, require extensive manual intervention, or rely on 2D edge heuristics that lack robustness and applicability across 3D volumetric data. This work, to the best of the authors' knowledge, is the first to present a generalized algorithm that automatically detects, segments, and quantitatively measures three-dimensional detonation cells using graph theory. The proposed method provides geometric structure of three-dimensional cells, vastly improving the ability to understand detonation structures. These findings will ultimately help improve practical detonation applications (rotating, pulse, oblique and standing detonation wave engines).

*Corresponding author.

1. Introduction

As detonation-based devices [1] were pioneered in the early 1950s, soot foils emerged as a diagnostic tool to visualize detonation front structures, such as wave collision points, to study intrinsic high-speed combustion and shock phenomena. These soot-coated substrates are placed along gaseous detonation channels that record triple-point tracks as the wave propagates, producing a “cellular lattice” imprint of the detonation front. Despite widespread use, these techniques are inherently two-dimensional, sampling only wall-adjacent dynamics and missing the full 3D front morphology. This motivates techniques to map the soot-foil lattice patterns to a 3D volumetric representation with minimal human effort.

Several techniques have been developed to quantify the cellular pattern on 2D soot foils [2–6]. Shepherd et al. [7] proposed a PSD-based cell-size estimator coupled with edge detection, linking pattern periodicity to dominant spatial frequencies via 2D Fourier analysis. Subsequent workflows and software packages popularized this route but retained substantial manual tuning. Carter et al. [3] extracted directional gradients with manual input to overlay binary cell maps while Ng et al. [5] performed CH*-based extraction of soot-foil-like patterns and then measured λ (characteristic cell width) with tools derived from Shepherd et al. [8]. Siatkowski et al. [9] showed CAD-assisted line plotting on foils and later trained model on curated databases to predict λ . Neural network approaches have since expanded, using larger datasets to predict λ from image features, though segmentation of irregular lattices remains challenging. Although recent approaches in computer vision [6] leverage contour-based segmentation, these methods are brittle in the presence of practical irregularities and topological defects. In contrast, our previous study [10] established a generalizable machine learning (ML) framework based on cellular biology models and validated its efficacy with rigorous benchmarks that exceed baseline techniques [6, 8].

Across these methods, the lattice pattern is treated as a 2D tessellation without any depth, while true 3D morphology is closer to practical systems. Monnier et al. [11] used soot-plate experiments with front-view and longitudinal recordings, showing longitudinal traces alone can misrepresent the full front; they proposed tessellation/Voronoi-based measures for an average cell width but note irreducible counting uncertainty and the reduction of 3D structure to 2D imprints. Later, Monnier et al. [12] used a graph-theoretic framework that infers a pseudo-3D cell width from 2D front-view detonation patterns, linking polygonal lattices to a volumetric scale without directly measuring the lattice itself. Borisov & Kudryavtsev [13] characterized 3D detonation cells using high-fidelity numerical simulations guided by linear instability theory: predicted transverse wavelengths were compared with simulation fields, cell evolution was quantified via Fourier analysis of trans-

verse velocity, and triple-point paths were visualized using maximum-pressure isosurfaces (“spatial smoke foils”). Their main limitations were acknowledged resolution constraints for early/small cells and simplified chemistry. Although high-fidelity simulations can generate 3D volumetric cellular fields [14–18], to our knowledge, there is no direct procedure that reconstructs or measures a 3D structure directly from detonation lattice data. The focus of this work is to bridge this gap by developing an algorithm that (i) robustly segments 3D lattice patterns, (ii) quantify anisotropy/regularity beyond λ , and (iii) is consistent with physics-based constraints. The algorithm is a generalizable, minimally supervised approach that captures 3D lattices from volumetric data. The following sections detail the algorithm for graph construction (§2.2) followed by results of the lattice case (§3.1) and a 3D numerical detonation lattice (§3.2).

2. Methodology

Graph representations provide mathematically rigorous encoding of interaction topology in natural systems, enabling statistically robust inference and analysis [19]. A graph provides a physically meaningful surrogate for the underlying 3D detonation lattice: nodes correspond to triple point collision kernels, while edges represent the intervening segments (Mach stems and incident shocks) oriented along wave motion (see Fig. 1). This abstraction preserves the essential topology—adjacency, branching, and cycles—that governs cell formation, irrespective of geometric distortions in any particular view. A graph built from these elements concisely should encode the 3D organization of the front: local motifs (Y-junctions, loops) assemble into a global lattice whose statistics (degree, cycle length, path structure) map to cell size, anisotropy, and interaction frequency.

2.1. Volumetric data segmentation

Building on our prior work [10], we implement a slice-wise volumetric segmentation workflow: the 3D field is decomposed into an ordered stack of 2D slices, each undergoes targeted preprocessing (denoising, contrast normalization, structure-enhancing filters) to suppress noise and amplify interfaces, and the preprocessed sequence, preserving slice order, is passed to a Segment-anything-style (SAM) model for inference [20, 21]. SAM-based foundation models provide strong, reusable visual representations for segmentation across diverse image distributions [20, 22]. Cellpose-SAM repurposes the pretrained SAM image encoder but replaces sequential mask decoding with Cellpose’s dense flow-field formulation, enabling efficient instance segmentation and straightforward extension to 3D by averaging predictions across XY/ZY/YZ slices before performing 3D mask dynamics [21]. While this architecture is attractive for automated cell-pattern extraction, at the same time, for strictly 2D detonation-cell post-processing

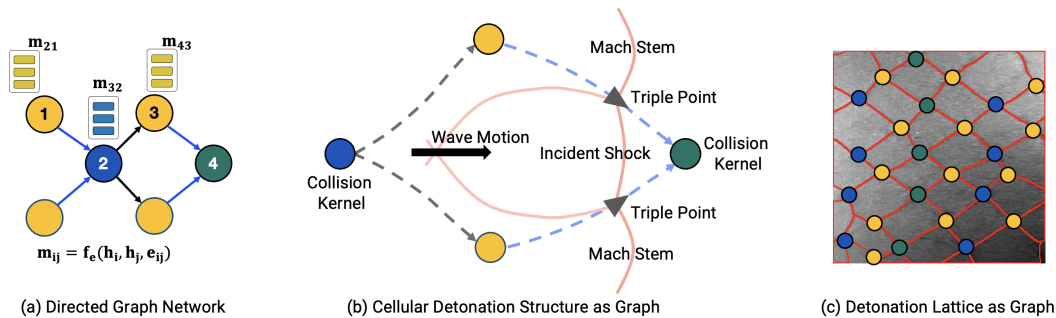


Fig. 1: Relating graph message passing to cellular detonation structure: (a) Directed message-passing graph: node features h_i exchange edge (e_{ij}) messages m_{ij} , (b) Cellular detonation interpreted as a graph: triple points and collision kernels serve as nodes connected along Mach stems and incident shocks; wave motion induces directional interactions and (c) 2D detonation lattice as a graph, with collisions points as nodes and wave path as edges, illustrating how collisions localize within the network.

(e.g., soot-plate or planar visualizations), deploying a large foundation model can be unnecessary overhead; models such as “cyto3” pipelines [10] may be sufficient when the goal is a single cell-size metric rather than general-purpose segmentation. Also noted in [21], direct comparison between Cellpose3 (cyto3) and CellSAM on datasets both were trained on, “*cyto3 performs better on every dataset*”. Thus, careful consideration is required before deploying such models: for 2D soot-foil analysis, lighter non-SAM pipelines are often sufficient and preferable due to their smaller memory footprint. In contrast, for volumetric segmentation tasks, SAM-based approaches can offer improved robustness and accuracy relative to the CNN-based models [10, 21].

Following initial analysis, SAM-based design enables flexible, multi-resolution operation across volumes of varying size and voxel aspect ratio while preserving fidelity to the underlying 3D morphology. The model returns a set of masks that uniquely label each cell, assigning a distinct integer ID to every voxel within each node (and across nodes when aggregated). The uniquely marked cluster is approximated by its centroid, i.e., the coordinate-wise average of the distance-transform-weighted center and the largest-inscribed-sphere (LIS) center [23]. This choice is critical because it mitigates bias from thin protrusions and irregular boundaries while preserving the true interior of the cell cluster.

2.2. Graph construction

From §2.1, given labeled 3D centroids $C \in \mathbb{R}^{N \times 3}$ with integer instance labels L (using SAM model and LIS centers), a sparse undirected graph is constructed by proposing edges only *forward* along a user-chosen axial direction $D \in \{\pm X, \pm Y, \pm Z\}$ (typically aligned with the wave propagation), followed by local pruning and degree capping. The detailed pseudo-code is presented in Algorithm 1. Each centroid is discretized into rectilinear bin coordinates (I, J, K) using user-defined grids (u_x, u_y, u_z) , and the direction D induces an axial index $A \in$

$\{I, J, K\}$, lateral indices (U, V) , and a sign $\text{sgn} \in \{+1, -1\}$.

Nodes are processed in lexicographic order consistent with sgn ; an optional reverse pass is included to reduce ordering bias. For a root node i , a candidate node j is considered only if it satisfies: (i) strict axial advance $\text{sgn}(A_j - A_i) > 0$; (ii) bounded axial span $|A_j - A_i| \leq A_{\max}$; and (iii) bounded lateral offset $|U_j - U_i| + |V_j - V_i| \leq R_{\text{side}}$. Remaining candidates are ranked by increasing axial separation and then lateral distance (with axial separation taken as either $|A_j - A_i|$ in bin units or $(C_j - C_i) \cdot \hat{d}$ in continuous units, depending on implementation), and the top K candidates are retained.

Edges are greedily accepted from the ranked short-list subject to a per-node degree cap deg_{\max} and duplicate suppression (undirected edges are stored as $(\min(i, j), \max(i, j))$). Two optional geometric tests further filter edges: (a) a *proximity* test (CLUSTER) that requires each endpoint centroid to lie within a threshold τ of voxels belonging to the other endpoint’s label, implemented with per-label KD-trees; and (b) an *occupancy* test (BETWEEN) that samples points along the segment (C_i, C_j) at a step size proportional to the minimum grid spacing and requires a minimum hit fraction ϕ_{\min} of sampled locations to fall within a voxel radius r_{vox} of any labeled voxel. In terms of physics, these constraints ensure that a wave must have traversed along/in the vicinity of the connecting path between nodes, ensuring that the edge is part of the original detonation lattice structure and suppress spurious long-range connections. Figure 2 illustrates the occupancy test: from a given root centroid, a Euclidean neighborhood search identifies the top beam-search candidates (C_1 to C_4) in the forward direction. Proposed edges are then screened with an occupancy (between-voxels) constraint that checks whether the segment lies within labeled structure along its path. Candidates that satisfy this physical-consistency test are retained (green), while spurious connections lacking supporting occupancy are rejected (red). With the top- K shortlist and the degree

cap, the resulting graph has $\mathcal{O}(N)$ edges, while KD-tree queries keep the optional test costs sublinear in the number of labeled voxels.

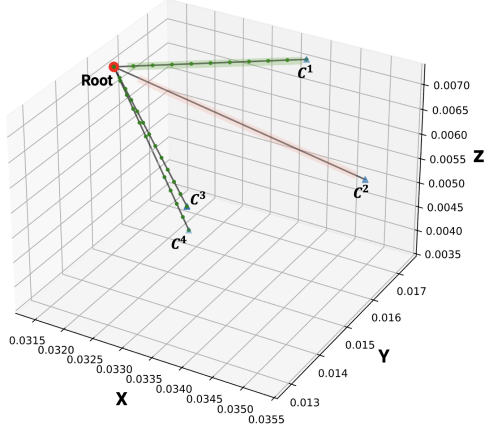


Fig. 2: Search in Euclidean space: a root node proposes its top four beam-search candidates; after applying occupancy constraints, only the green-marked (physically consistent) candidates are accepted, while the red-marked is rejected.

3. Results and Discussion

The first-subsection discusses results for a manufactured problem and the latter subsection measures and approximates a 3D detonation lattice using the said graph algorithm.

3.1. Generated lattice

To assess volumetric segmentation and detection efficacy, a synthetic 3D dataset with a fixed geometric arrangement of tightly packed, ellipsoid-like volumes was constructed (Fig. 3). The objects are arranged on a regular lattice with minimal inter-object spacing to induce frequent contacts and occlusions, thereby increasing segmentation difficulty. Experiments vary only the input sampling to the model, the “cell count” per axis of the volumetric grid (n_x), while keeping the underlying geometry unchanged (base geometry defined at $n_x=240$). Input resolutions range from 60 to 480 voxels per axis (Fig. 3), providing a controlled progression from coarse to refined sampling to quantify how much structure is recoverable as discretization improves.

Table 1: Effect of cell count (n_x) on prediction error (%) (top row), the size of the lattice file (middle row) and number of masks generated by the model (bottom row).

060	120	240	480
14.23 ± 2.37	14.62 ± 1.31	02.38 ± 0.19	00.73 ± 0.49
0.66 MB	5.20 MB	41.50 MB	331.90 MB
60	60	60	1101

From Table 1, prediction error remains high at coarse samplings (14.23% at 60; 14.62% at 120, see

Algorithm 1 Lattice Graph Construction

Require: $C \in \mathbb{R}^{N \times 3}$, L ; grids u_x, u_y, u_z ; axis, A_{\max} , R_{side} , K , deg_{\max} ; optional gates: $\text{CLUSTER}(\tau)$, $\text{BETWEEN}(s_{\text{vox}}, r_{\text{vox}}, \phi_{\min})$

- 1: **Map** axis \rightarrow (ax, sgn, u, v); **bin:** $I = \text{bin}(C_x, u_x)$, $J = \text{bin}(C_y, u_y)$, $K = \text{bin}(C_z, u_z)$; $A = [I, J, K]_{\text{ax}}$, $U = [I, J, K]_u$, $V = [I, J, K]_v$
- 2: $O_{\text{fwd}} \leftarrow$ lexicographic order for sgn; $\mathcal{O} \leftarrow [O_{\text{fwd}}]$ (optionally add reverse); **init** $\text{deg}=0$, $\mathcal{E} = \emptyset$, $\mathcal{S} = \emptyset$; **prebuild** KD-trees if gates enabled; **set** s, r from $s_{\text{vox}}, r_{\text{vox}}$
- 3: **for** $O \in \mathcal{O}$ **do**
- 4: **for** $i \in O$ **do**
- 5: **if** $\text{deg}[i] = \text{deg}_{\max}$ **then continue**
- 6: **end if**
- 7: $\mathcal{C} \leftarrow \emptyset$;
- 8: **for** $j = 1..N$, $j \neq i$ **do**
- 9: $dA = A[j] - A[i]$;
- 10: **if** $\text{sgn } dA \leq 0$ or $|dA| > A_{\max}$ or $|U[j] - U[i]| + |V[j] - V[i]| > R_{\text{side}}$ **then continue**
- 11: **end if**
- 12: **Push** $(j, \Delta_{\text{ax}}(i, j), \text{lat}(i, j))$ to \mathcal{C}
- 13: **end for**
- 14: **Sort** \mathcal{C} by $(\Delta_{\text{ax}} \uparrow, \text{lat} \uparrow)$; **keep** first K
- 15: **for** $(j, \cdot, \cdot) \in \mathcal{C}$ **do**
- 16: **if** $\text{deg}[i] = \text{deg}_{\max}$ or $\text{deg}[j] = \text{deg}_{\max}$ **then continue**
- 17: **end if**
- 18: $e = (\min(i, j), \max(i, j))$;
- 19: **if** $e \in \mathcal{S}$ **then continue**
- 20: **end if**
- 21: **if** CLUSTER on **then** reject if $\min\{d(\text{KD}_{L[j]}, C[i]), d(\text{KD}_{L[i]}, C[j])\} > \tau$
- 22: **end if**
- 23: **if** BETWEEN on **then** let $\phi = \text{HITFRAC}(C[i], C[j]; \text{KD}_U, s, r)$;
- 24: **if** $\phi < \phi_{\min}$ **then continue**
- 25: **end if**
- 26: **end if**
- 27: **Append** $(i, j, \|C[j] - C[i]\|_2)$ to \mathcal{E} ; **insert** e into \mathcal{S} ; $\text{deg}[i] += 1$; $\text{deg}[j] += 1$
- 28: **end for**
- 29: **end for**
- 30: **end for**
- 31: **return** \mathcal{E} , deg

Fig. 3(a)), then drops sharply near the native geomet-

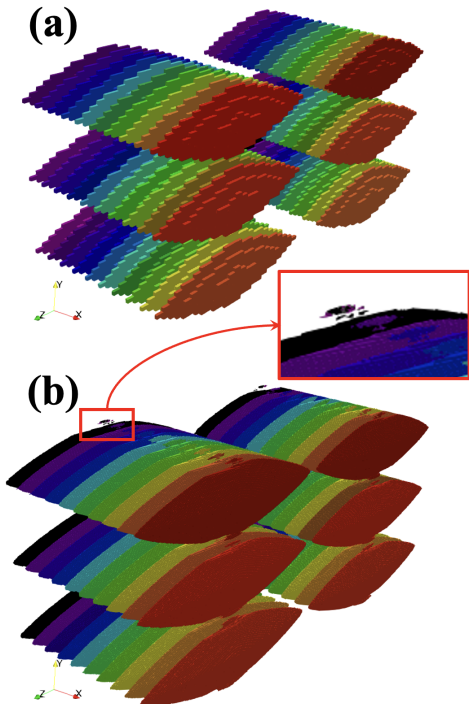


Fig. 3: Plot for 3-D generated lattice segmented by the model: (a) $n_x=60$ and (b) $n_x=480$. Red box shows mask fragmentation due to over-segmentation in $n_x=480$ case.

ric scale (2.38% at 240) and reaches its lowest value at 480 (0.73%). File size grows approximately cubically with resolution—0.66 MB to 331.90 MB—reflecting the volumetric scaling law. Notably, mask proliferation is negligible until 480 cells per axis (60 masks at 60 to 240 versus 1101 at 480), indicating over-segmentation emerges only at the finest input sampling. Overall, sampling near the base geometry ($n_x=240$) captures structure accurately with modest storage, while 480 offers marginal error gains at substantially higher storage and a risk of excessive mask fragmentation (see Fig. 3(b)).

3.2. 3D Detonation simulation based reconstruction

The algorithm is evaluated on 3D lattice fields generated from a gaseous detonation simulation of a stoichiometric ethylene–air mixture at a pre-detonation temperature of 500 K and pressure of 1 atm. The one-dimensional induction length for this mixture is $l_{ind} = 516 \mu\text{m}$. The finest grid spacing is $9.766 \mu\text{m}$, which yields about 52 cells per induction length. This resolution is sufficient to resolve the cellular detonation structure, including triple points, Mach stems, and collision zones, ensuring a sufficiently reliable representation of the underlying physics. Additional details are discussed in [24].

Following the workflow in Fig. 6, the detonation lattice is first extracted by tracking the maximum

pressure observed by each cell in the numerical domain (plot (a)). This data is stored as a point-based structured grid which is then sliced along the transverse direction for the segmentation model to process. The output of the SAM model assigns a unique ID to a cluster of cells as discussed in §3.1 (plot (b)). To construct the graph, each cell cluster is mapped to a unique point that is both interior and boundary-aware (plot (c)). This step is essential as it determines the collision sites in the lattice that define the shape’s boundary points. The edges are subsequently constructed between these nodes (plot (d)) using the algorithm in §2.2 to obtain the 3D cell (plot (e)). All physical quantities are reported in the mesh’s native coordinate units; no unit conversion was applied. The measurements are computed directly from the geometry of the closed surface (vertex positions and triangulated faces), not from a voxel/grid discretization, i.e., no voxels are used.

Fig. 4 shows the one-dimensional distributions (from 25 samples) of the lengths of the major and minor axes (mesh units) in plots (a), (b) and (b): the teal curve is a kernel density estimate (KDE) (normalized with peak value); all features appear unimodal. The cell geometry is systematically elongated in the X-axis with moderate variability in length scales but substantial variability in volume. The distribution of the major axis (L_x) centers near 0.00839 (median), with a slightly larger mean (0.00851) and a fairly narrow spread in the middle. The negative skew is evident with a longer left tail: few smaller samples deviate trend to the low-end. However, most samples lie in a narrow band around 0.008–0.009. In contrast, minor axis (L_y) distribution is more concentrated around its center (median = 0.00403) and only slightly right-skewed: the mean (0.00403) essentially matches the median, with a few modestly larger values. A similar trend follows for L_z distributions with a median around 0.005 slightly larger than the mean ≈ 0.0048 . Table 2 reports different statical measures (from Fig. 4) for cell lengths (L) along each axis and the geometric volume of the 3D cell. The coefficients of variation (σ/μ) are modest for lengths, approx. 15–17% across the three L s. In contrast, volume is highly dispersed, indicating a typical pattern when small differences in linear size propagate cubically into volume. For all three lengths, $M > \mu$, suggesting a slight right-skew (few larger values). Volume shows the opposite trend, indicating a left-skewed distribution, consistent with multiplicative variation in size.

Table 2: Summary statistics: the mean (μ), standard deviation (σ), and median (M) of the extents L_x , L_y , L_z and V (volume) for 25 samples in native units of the mesh.

Measure	L_x	L_y	L_z	V
μ	8.36e-3	5.30e-3	4.82e-3	2.11e-7
σ	12.82e-4	7.88e-4	8.09e-4	2.36e-7
M	8.55e-3	5.33e-3	5.01e-3	1.33e-7

Figure 5 shows the joint distribution of volume

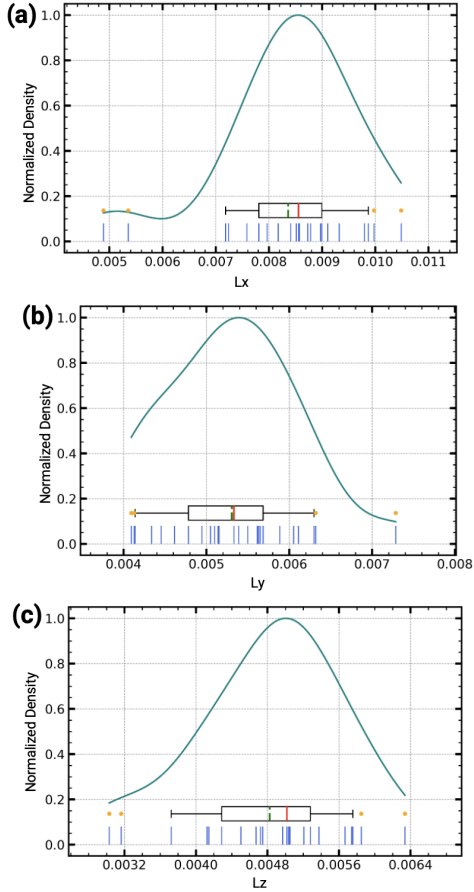


Fig. 4: Plot of geometric features from 25 samples: (a) major-axis length, (b) minor-axis length, each shown as a KDE (normalized) with stick marks indicating individual samples (blue) and an inline boxplot (median = red line, mean = green dashed line, whiskers 5th–95th percentiles); (c) joint density of volume and aspect ratio (major/minor axis) with overlaid points (normalized density color scale).

(log-scale) with different aspect ratios (AR), where contours represent normalized density and orange dots are the samples. Plots (a) and (b) show that most shapes cluster at intermediate volumes with moderate aspect ratios (1.6 to 2.2), with lighter contours (and scattered points) extending toward larger volumes and higher aspect ratios. This observation is consistent with the elongation of X-axis over Y and Z. The plot (c) for AR₃ is clustered close to 1.0–1.2, implying Y and Z extents are comparatively similar, as observed by Oladipo et al. [24]. Across all three, the contours are broadly ellipsoidal with only a slight tilt, suggesting at most a weak dependence of aspect ratio on volume: larger volumes do not strongly skew the AR, though the highest densities sit at intermediate volumes and moderate anisotropy.

4. Conclusion

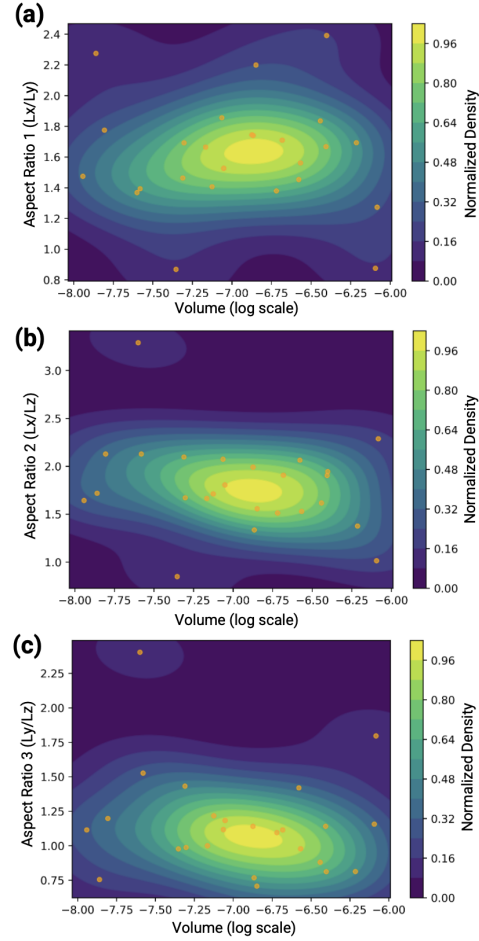


Fig. 5: Plot of joint density of volume and aspect ratio (AR) from 25 samples with overlaid points (normalized density color scale): (a) $AR_1=L_x/L_y$, (b) $AR_2=L_x/L_z$ and (c) $AR_3=L_y/L_z$.

A graph-based framework using SAM-model was developed to analyze and quantify the three-dimensional morphology of detonation cells. Evaluated with controlled lattice test cases that mimic detonation-cell volumes, the model predicts cell volume within 2% error, supporting the reliability of the end-to-end pipeline. The framework was then applied to 3D numerical data to extract statistical measures for axial length scales (L_x, L_y, L_z), cell volume V , and their joint distributions. The resulting length distributions are unimodal and indicate systematically elongated cells along the x -direction, with modest variability in the linear extents (coefficients of variation ≈ 15 –17%). In contrast, V exhibits substantially larger dispersion, consistent with cubic amplification of small variations in length. Joint PDFs of V and aspect ratios show clustering at intermediate volumes with moderate anisotropy ($AR \approx 1.6$ –2.2) and weak coupling between aspect ratio and volume, while the

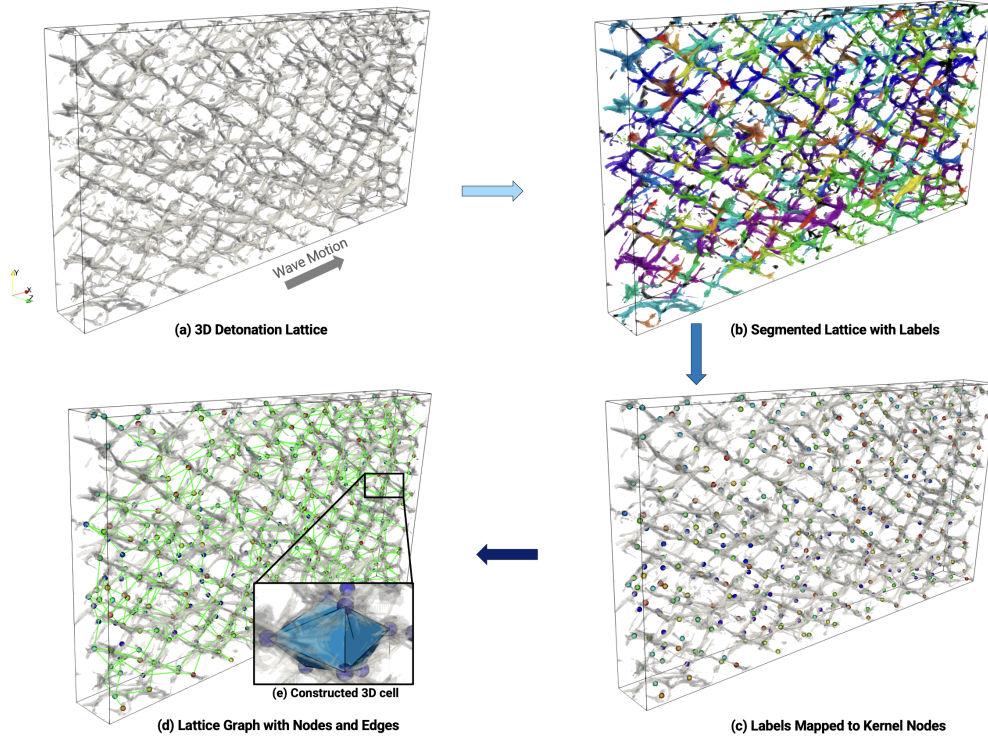


Fig. 6: Overall workflow of the segmentation and graph construction procedures on a 3D numerical detonation lattice.

extents of $y-z$ remain comparatively similar. Overall, the method provides robust, physically interpretable 3D cell statistics suitable for subsequent studies of confined triple-point interactions and the growth of cellular instabilities.

CRediT authorship contribution statement

VS: designed research, developed software, performed research, analyzed data, wrote—original draft, review and editing. **VR:** designed research, developed software, analyzed data, wrote—review and editing, project administration, funding acquisition.

Declaration of competing interest

The authors declare that they have no known competing financial interests or personal relationships that could have appeared to influence the work reported in this paper.

Acknowledgments

The authors acknowledge support from Air Force Office of Scientific Research (AFOSR) under Grant No. FA9550-24-1-0017, with Dr. Chiping Li as Program Officer. The authors thank Abiola Oladipo for providing 3D detonation data.

References

- [1] J. A. Nicholls, H. Wilkinson, R. B. Morrison, Intermittent detonation as a thrust-producing mechanism, *Journal of jet propulsion* 27 (5) (1957) 534–541.
- [2] A. P. Nair, A. R. Keller, N. Q. Minesi, D. I. Pineda, R. M. Spearrin, Detonation cell size of liquid hypergolic propellants: Estimation from a non-premixed combustor, *Proceedings of the Combustion Institute* 39 (3) (2023) 2757–2765.
- [3] M. Carter, D. L. Blunck, Direct comparison of schlieren and soot foil measurements of detonation cell sizes, *Frontiers in Aerospace Engineering* 1 (2022) 892330.
- [4] J. Shepherd, I. Moen, S. Murray, P. Thibault, Analyses of the cellular structure of detonations, in: *Symposium (International) on Combustion*, Vol. 21, Elsevier, 1988, pp. 1649–1658.
- [5] B. M. Ng, E. N. Hoffman, D. I. Pineda, C. S. Combs, Detonation cell size estimation via chemiluminescence imaging in an optically accessible linear detonation tube, *Experiments in Fluids* 65 (7) (2024) 108.
- [6] D. Jalontzki, A. Zussman, S. Pendurkar, G. Sharon, Y. Kozak, A computer vision approach for analysis of detonation cellular structures, *Applications in Energy and Combustion Science* (2025) 100340.
- [7] J. E. Shepherd, Detonation in gases, *Proceedings of the Combustion Institute* 32 (1) (2009) 83–98.
- [8] J. Lee, D. Garinis, D. Frost, J. Lee, R. Knystautas, Two-dimensional autocorrelation function analysis of smoked foil patterns, *Shock Waves* 5 (1995) 169–174.
- [9] S. Siatkowski, K. Wacko, J. Kindracki, Predicting detonation cell size of biogas–oxygen mixtures using machine learning models, *Shock Waves* (2024) 1–9.
- [10] V. Sharma, M. Ullman, V. Raman, A machine learning based approach for statistical analysis of detonation cells from soot foils, *Combustion and Flame* 274 (2025) 114026.
- [11] V. Monnier, V. Rodriguez, P. Vidal, R. Zitoun, An analysis of three-dimensional patterns of experimental detonation cells, *Combustion and Flame* 245 (2022) 112310.
- [12] V. Monnier, P. Vidal, V. Rodriguez, R. Zitoun, From graph theory and geometric probabilities to a representative width for three-dimensional detonation cells, *Combustion and Flame* 256 (2023) 112996.
- [13] S. Borisov, A. Kudryavtsev, Investigation of cellular detonation structure formation via linear stability theory and 2d and 3d numerical simulations, in: *AIP Conference Proceedings*, Vol. 1893, AIP Publishing LLC, 2017, p. 030042.
- [14] D. N. Williams, L. Bauwens, E. S. Oran, Detailed structure and propagation of three-dimensional detonations, in: *Symposium (International) on Combustion*, Vol. 26, Elsevier, 1996, pp. 2991–2998.
- [15] J. Crane, J. T. Lipkowitz, X. Shi, I. Wlokas, A. M. Kempf, H. Wang, Three-dimensional detonation structure and its response to confinement, *Proceedings of the combustion institute* 39 (3) (2023) 2915–2923.
- [16] K. Iwata, S. Suzuki, R. Kai, R. Kurose, Direct numerical simulation of detonation–turbulence interaction in hydrogen/oxygen/argon mixtures with a detailed chemistry, *Physics of Fluids* 35 (4) (2023).
- [17] N. Tsuboi, S. Katoh, A. K. Hayashi, Three-dimensional numerical simulation for hydrogen/air detonation: Rectangular and diagonal structures, *Proceedings of the Combustion Institute* 29 (2) (2002) 2783–2788.
- [18] S. Abisleiman, V. Sharma, R. Bielawski, V. Raman, Structure of three-dimensional conical oblique detonation waves, *Combustion and Flame* 274 (2025) 113971.
- [19] A. Sanchez-Gonzalez, J. Godwin, T. Pfaff, R. Ying, J. Leskovec, P. Battaglia, Learning to simulate complex physics with graph networks, in: *International conference on machine learning*, PMLR, 2020, pp. 8459–8468.
- [20] A. Kirillov, E. Mintun, N. Ravi, H. Mao, C. Rolland, L. Gustafson, T. Xiao, S. Whitehead, A. C. Berg, W.-Y. Lo, et al., Segment anything, in: *Proceedings of the IEEE/CVF international conference on computer vision*, 2023, pp. 4015–4026.
- [21] M. Pachitariu, M. Rariden, C. Stringer, Cellpose-sam: superhuman generalization for cellular segmentation, *bioRxiv* (2025) 2025–04.
- [22] N. Ravi, V. Gabeur, Y.-T. Hu, R. Hu, C. Ryali, T. Ma, H. Khedr, R. Rädle, C. Rolland, L. Gustafson, et al., Sam 2: Segment anything in images and videos, *arXiv preprint arXiv:2408.00714* (2024).
- [23] H. S. M. Coxeter, *Regular polytopes*, Courier Corporation, 1973.
- [24] A. Oladipo, S. S. Abisleiman, V. Sharma, J. Singh, V. Raman, S. Dwivedi, T. Hedman, Three observations on cell formation in confined detonations, *Manuscript under review* (2025).